

Crystal structure of Mo-substituted lanthanum tungstate $\text{La}_{5.4}\text{W}_{1-y}\text{Mo}_y\text{O}_{12-\delta}$ ($0 \leq y \leq 0.2$) studied by X-ray and neutron diffraction

Andrea Fantin,^{a*} Tobias Scherb,^a Janka Seeger,^b Gerhard Schumacher,^a Uta Gerhards,^c Mariya E. Ivanova,^b Wilhelm A. Meulenberg,^b Roland Dittmeyer^c and John Banhart^{d,e}

Received 1 October 2018

Accepted 29 June 2019

Edited by D. Pandey, Indian Institute of Technology (Banaras Hindu University), Varanasi, India

Keywords: Mo-substituted lanthanum tungstates; mixed protonic–electronic conductors; high-resolution X-ray diffraction; neutron diffraction; electron-probe micro-analysis.

CCDC reference: 1937552

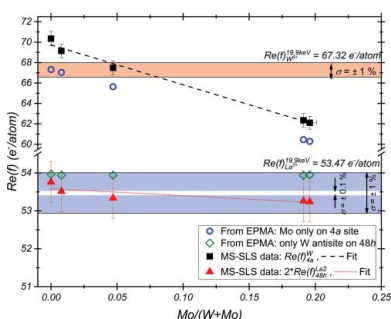
Supporting information: this article has supporting information at journals.iucr.org/j

^aDepartment of Microstructure and Residual Stress Analysis, Helmholtz-Zentrum-Berlin GmbH, Hahn-Meitner-Platz 1, Berlin 14109, Germany, ^bInstitute of Energy and Climate Research, Forschungszentrum Jülich GmbH, Jülich 52425, Germany, ^cInstitute for Micro Process Engineering, Karlsruhe Institute of Technology, Hermann-von-Helmholtz-Platz 1, Eggenstein-Leopoldshafen 76344, Germany, ^dDepartment of Applied Materials, Helmholtz-Zentrum-Berlin GmbH, Hahn-Meitner-Platz 1, Berlin 14109, Germany, and ^eTechnical University of Berlin, Hardenbergstrasse 36, Berlin 10623, Germany. *Correspondence e-mail: andrea.fantin@helmholtz-berlin.de

A determination of the detailed crystal structure of an Mo-substituted lanthanum tungstate series, $\text{La}_{6-x}\text{W}_{1-y}\text{Mo}_y\text{O}_{12-\delta}$ ($0 \leq y \leq 0.2$, δ is the oxygen deficiency), is presented. Material of composition $\text{La}_{5.4}\text{W}_{0.8}\text{Mo}_{0.2}\text{O}_{12-\delta}$ ($y = 0.2$) produced by the citrate-complexation route based on the Pechini method was investigated by high-resolution X-ray diffraction and neutron diffraction in the temperature range $10 \leq T \leq 298$ K. The results are compared with a non-substituted material $\text{La}_{5.4}\text{WO}_{12-\delta}$. A structural model established earlier for lanthanum tungstates and Re-substituted lanthanum tungstates is confirmed, according to which the Wyckoff site shared by La and W is split with half site occupancies ($Fm\bar{3}m$ space group, $48h$ site) and also accommodates Mo atoms. Substitution of W by up to 20 mol% Mo does not change the face-centred cubic lattice: Mo atoms substitute W statistically on both $4a$ and $48h$ Wyckoff sites of the crystal structure, which is described by the $Fm\bar{3}m$ space group. These results were obtained from the combination of the average neutron-scattering length and average X-ray scattering power procedures with electron-probe micro-analysis. The temperature dependence of bond lengths in dry and wet (D_2O) conditions shows that vacant oxygen sites are located on the $32f$ Wyckoff sites also in Mo-substituted lanthanum tungstates, and that the bond lengths between La on $4b$ and O on $32f$ increase with increasing $p\text{O}_2$ and $p\text{D}_2\text{O}$, reflecting the filling of oxygen vacancies and the increase in coordination of La on $4b$.

1. Introduction

Hydrogen-related technologies have been of increasing interest during recent years, for instance to reduce the consumption of fossil fuel and the release of greenhouse gases. H_2 could be exploited as an energy carrier (Sorensen, 2007; Kim *et al.*, 2008; Genovese *et al.*, 2011; Niknam *et al.*, 2013). It could be produced in different ways, through clean sources such as electrolysis (Zeng & Zhang, 2010) or fossil-fuel-related sources, *e.g.* methane steam reforming (Simpson & Lutz, 2007) or coal gasification (Lin, 2002). Employing fossil fuels for hydrogen production is still economically favourable but needs H_2 separation from flue gases such as CO_x , NO_x and SO_x . One of the ways to achieve H_2 separation is to use hydrogen-permeable membranes. The main requirements for such membranes could be identified as high H_2 selectivity, mechanical stability and durability under exposure to flue-gas-containing atmospheres, and large ambipolar conductivity (Norby, 2000; Fontaine *et al.*, 2007; Norby & Haugsrud, 2008).



© 2019 International Union of Crystallography

Different materials could be employed to build these membranes, for instance alkaline-earth-based oxides with a perovskite structure (Norby, 1999; Iwahara *et al.*, 1981; Iwahara, 1988). Amongst these oxides, barium-based perovskites can achieve high performance [barium cerates (BCO) (Iwahara *et al.*, 1981; Iwahara, 1988)] or high stability [barium zirconates (BZO) (Haile *et al.*, 2001)]. However, BCO is unstable in CO/CO₂-containing atmospheres, while BZO has a high sintering temperature and large electrical resistivity. Even though various substitutions on *A* and *B* sites in BCO and BZO are being developed (Kjølseth *et al.*, 2010; Dahl *et al.*, 2011; Ricote *et al.*, 2011; Magrasó *et al.*, 2012), as well as ceramic composites (Rebollo *et al.*, 2015; Ivanova *et al.*, 2016), another class of materials has aroused interest for its high protonic conductivity and its stability in harsh atmospheres, namely rare-earth-based tungsten oxides (LnWO, where Ln is a rare earth element). Such materials with Ln = La or Nd could be used as electrolytes in fuel cells because of their almost pure protonic conductivity at low and intermediate temperatures (Haugrud, 2007; Magrasó, 2013; Quarez *et al.*, 2013). Poor electronic conductivity is a drawback of these materials for applications as hydrogen-permeating membranes. However, partial substitution of W by Re or Mo was shown to increase the performance of LnWO at intermediate temperatures by up to a factor of 10 (Escolastico *et al.*, 2013; Seeger *et al.*, 2013; Escolástico *et al.*, 2014). Substitution of W by Mo (Escolastico *et al.*, 2013; Escolástico *et al.*, 2015; Magrasó & Frontera, 2016) or co-substitution of Mo and Nb for W (Chen *et al.*, 2016) have led to improvements in hydrogen-permeation fluxes. This is because of the higher reducibility of the substituted cations compared with W, as the latter maintains its 6+ oxidation state even in very reducing atmospheres (Erdal *et al.*, 2012; Escolastico *et al.*, 2013). Understanding the crystal structure of LnWO-based materials is crucial for their further development and application. Among the different structural models proposed for the non-substituted LaWO (LWO) system, different publications reported the same crystal structure (Fantin *et al.*, 2016; Scherb *et al.*, 2016; Magrasó & Frontera, 2016). In addition, some reports on the crystal structure of Nb-, Mo- and Re-substituted lanthanum tungstates have proposed a structural model similar to that for the non-substituted LWO (Magrasó & Frontera, 2016; Fantin *et al.*, 2016), except for Nb-substituted LWO (Zayas-Rey *et al.*, 2013). Further investigation of the crystal structure of Mo-substituted LWO is the focus of our work: through temperature-dependent neutron diffraction and high-resolution X-ray diffraction (HRXRD), a thorough study on the structure of a series of Mo-substituted LWO compounds (La_{5.4}W_{1-y}Mo_yO_{12-δ}; 0 ≤ y ≤ 0.2) is performed.

2. Experimental

2.1. Samples

2.1.1. Synthesis. The sample series La_{5.4}W_{1-y}Mo_yO_{12-δ} (0 ≤ y ≤ 0.2, where y represents the substitution of W by Mo and δ describes the oxygen deficiency) was prepared through the

citrate-complexation route based on the Pechini reaction (Pechini, 1967). The use of the citrate-complexation route for the production of La_{5.4}W_{1-y}Mo_yO_{12-δ} (0 ≤ y ≤ 0.2) is described by Seeger *et al.* (2013). After the pellets were sintered, conventional X-ray diffraction (XRD) measurements were performed in order to check for possible surface contaminations. If small amounts of a secondary phase on a specimen surface were found, the specimen was polished until the unwanted contamination could no longer be detected by XRD measurements.

2.1.2. Pre-treatment: dry/wet specimens. The samples were pre-treated in a furnace under a continuous flow of dried or humidified (with D₂O) atmospheres in Al₂O₃ holders (50 × 20 × 20 mm). The drying procedure was carried out under an argon stream (Ar) or synthetic air (SA) at 1173 K for 4 h. Humidifying atmosphere (2.5 vol.%) was supplied to the furnace by connecting two bubble bottles filled with D₂O to the Ar or SA pipe. In this case, the furnace was kept at 623 K for 5 h. Prior to the experiments, vanadium cans were filled with the specimen powders in a glovebox under Ar gas to preserve the pre-treatment.

2.1.3. Notations used. In the present work, samples labelled ‘dry(SA)’ or ‘dry(Ar)’ refer to samples dried under SA or Ar atmosphere, respectively. D₂O humidification performed under a stream of Ar gas or SA is referred to as D₂O(Ar) and D₂O(SA), respectively. The LWO specimen synthesized through a Pechini procedure is labelled as LWO_P, while the Mo-substituted LWO system is denoted as LW(Mo)O, and each specimen is labelled as Moz, where z denotes the nominal molar substitution of W by Mo in %.

2.2. Methods

2.2.1. Electron-probe micro-analysis and thermogravimetry. The composition of the specimens was measured by electron-probe micro-analysis (EPMA) in a JEOL JXA 8530F field emission microprobe. A Netzsch TG209F1 Iris micro-balance equipped with a QMS 403 Aëolos mass spectrometer was used for thermogravimetric measurements to determine the water uptake of the specimens during heating. Details of EPMA and thermogravimetric measurements are reported elsewhere (Fantin *et al.*, 2017).

2.2.2. X-ray diffraction. XRD measurements were performed in Bragg–Brentano geometry with a Bruker D8 Advance instrument, equipped with a LYNXEYE detector and a nickel filter (0.5 μm). The characteristic radiation lines used are Cu Kα₁ (1.5406 Å) and Cu Kα₂ (1.5444 Å). Phase identification was carried out with the ICDD PDF2 database in the EVA14 software (Bruker, 2008).

2.2.3. Neutron diffraction. Neutron diffraction (ND) measurements at different temperatures were performed at various experimental stations: D2B (Hewat & Heathman, 1984) at the Institut Laue–Langevin (ILL) and HRPT (Fischer *et al.*, 2000) at the Paul Scherrer Institute (PSI). Diffractograms were recorded at 30, 60, 100, 150, 200 and 298 K (D2B, λ = 1.594 Å) and at T = 10 and 295 K (HRPT, λ = 1.494 Å), for both dry(Ar) and wet(D₂O) pre-treated specimens. At every

Table 1

Nominal and experimental composition (EPMA/XRD), phase-composition status, techniques used and sample labels as used throughout the article.

The pre-characterization of the LW(Mo)O specimen series with thermogravimetry (TG) and laboratory XRD results is published elsewhere (Fantin *et al.*, 2017).

Nominal composition	Experimental composition	Secondary phases	Techniques	Sample labels
$\text{La}_{5.4}\text{W}_{1-y}\text{Mo}_y\text{O}_{12-\delta}$ ($0 \leq y \leq 0.2$)			EPMA, XRD, TG, ND, HRXRD	LW(Mo)O
$\text{La}_{5.4}\text{WO}_{12-\delta}$	$\text{La}_{5.56(3)}\text{WO}_{12-\delta}$	No		LWO_P
$\text{La}_{5.4}\text{W}_{0.99}\text{Mo}_{0.01}\text{O}_{12-\delta}$	$\text{La}_{5.62(3)}\text{W}_{0.992(1)}\text{Mo}_{0.008(1)}\text{O}_{12-\delta}$	No		Mo1
$\text{La}_{5.4}\text{W}_{0.95}\text{Mo}_{0.05}\text{O}_{12-\delta}$	$\text{La}_{5.64(3)}\text{W}_{0.953(2)}\text{Mo}_{0.047(2)}\text{O}_{12-\delta}$	No		Mo5
$\text{La}_{5.4}\text{W}_{0.90}\text{Mo}_{0.10}\text{O}_{12-\delta}$	$\text{La}_{5.8(5)}\text{W}_{0.89(2)}\text{Mo}_{0.11(2)}\text{O}_{12-\delta}$	$\text{La}_6\text{W}_2\text{O}_{15}$ (<1 wt%) La_2O_3 (<2 wt%)	No ND, HRXRD	Mo10
$\text{La}_{5.4}\text{W}_{0.85}\text{Mo}_{0.15}\text{O}_{12-\delta}$	$\text{La}_{5.8(2)}\text{W}_{0.85(1)}\text{Mo}_{0.15(1)}\text{O}_{12-\delta}$	$\text{La}_6\text{W}_2\text{O}_{15}$ (<1 wt%) La_2O_3 (<1 wt%)	No ND, HRXRD	Mo15
$\text{La}_{5.4}\text{W}_{0.8}\text{Mo}_{0.2}\text{O}_{12-\delta}$	$\text{La}_{5.64(4)}\text{W}_{0.809(2)}\text{Mo}_{0.191(2)}\text{O}_{12-\delta}$	No		Mo20(1)
$\text{La}_{5.4}\text{W}_{0.8}\text{Mo}_{0.2}\text{O}_{12-\delta}$	$\text{La}_{5.64(7)}\text{W}_{0.803(7)}\text{Mo}_{0.197(7)}\text{O}_{12-\delta}$	$\text{La}_6\text{W}_2\text{O}_{15}$ (<1 wt%) La_2O_3 (<1 wt%)		Mo20(2)

experimental station and for every temperature, a vanadium can with a diameter of $\varnothing = 6$ mm was used because of its low coherent [$b_{\text{coh}}(\text{V}) = -0.44$ (1) fm] scattering. Depending on the pre-treatment, the wet(D_2O) specimens were measured at D2B (ILL) or at HRPT (PSI), at the above-mentioned temperatures. The $\text{D}_2\text{O}(\text{Ar})$ samples were measured at D2B in a cryo-cooler ($3.5 < T < 300$ K), while the $\text{D}_2\text{O}(\text{SA})$ pre-treated specimens were measured at HRPT using an orange cryostat equipped with a four-sample changer stick ($1.5 < T < 300$ K). Neutron absorption in transmission geometry was taken into account including $\mu R/\lambda$ values ($R = 3$ mm is the can radius and μ is the linear absorption coefficient). The packing density employed for calculating absorption was 4 g cm^{-3} , estimated as 0.6 times the crystallographic density. All the $\mu R/\lambda$ values were found to be close to 0.03 \AA^{-1} , depending on the wavelength and the specimen composition. The absorption corrections were kept fixed during the refinement procedure.

Structural refinements were carried out using the software *GSAS* with the *EXPGUI* graphical user interface (Toby, 2001; Larson & Von Dreele, 2004), and *TOPAS* (Evans, 2010; Coelho, 2018).

Results obtained previously on LW(Re)O samples had shown that Re atoms substitute W in both its Wyckoff sites, $4a$ and $48h$ (Fantin *et al.*, 2016). This is a consequence of the different neutron-scattering lengths of Re [$b_{\text{coh}}^{\text{Re}} = 9.2$ (2) fm] and W [$b_{\text{coh}}^{\text{W}} = 4.755$ (18) fm]. Their relative difference $(b_{\text{coh}}^{\text{Re}} - b_{\text{coh}}^{\text{W}})/b_{\text{coh}}^{\text{Re}} \simeq 48\%$ allows for a sufficiently high contrast to distinguish Re and W through ND. This feature is not as evident in LW(Mo)O specimens because of the smaller difference between the neutron-scattering length of Mo [$b_{\text{coh}}^{\text{Mo}} = 6.715$ (20) fm] compared with W [$b_{\text{coh}}^{\text{W}} = 4.755$ (18) fm] which results in a relative difference $(b_{\text{coh}}^{\text{Mo}} - b_{\text{coh}}^{\text{W}})/b_{\text{coh}}^{\text{Mo}} \simeq 29\%$. The method of the average neutron-scattering length (Furrer *et al.*, 2009; Stephan *et al.*, 2012) has been applied in the same fashion as for LW(Re)O (Fantin *et al.*, 2016). Concerning the other elements in the unit cell, La ($Z_{\text{La}} = 57$) has a coherent neutron-scattering length of 8.24 (4) fm, whilst the neutron-scattering length of oxygen ($Z_{\text{O}} = 8$) is 5.805 (4) fm, providing enough contrast between the different elements in the crystal structure to locate the oxygen atoms as well.

2.2.4. High-resolution X-ray diffraction. Synchrotron XRD is particularly suitable for investigating LW(Mo)O specimens because of the good contrast between Mo ($Z = 42$) and W ($Z =$

74). In HRXRD experiments, glass capillaries of diameter $\varnothing = 0.2$ mm were used when measuring in a cryostat, and glass capillaries of diameter $\varnothing = 0.1$ mm were used when measuring with a cryojet and without any sample environment. Specimens filled into capillaries with diameter $\varnothing = 0.2$ mm were diluted with silicon powder (Si640d NIST) to reduce absorption effects, as too much X-ray absorption of the materials can compromise data quality, and for calibration purposes, as the capillary may slightly move with temperature variation. The dilution percentage was calculated according to NIST guidelines at the X-ray energy used at the experimental station (19.9 keV). Some specimens were measured once more at the MS beamline [Swiss Light Source (SLS), PSI; Willmott *et al.*, 2013] with HRXRD at a later stage ($T = 295$ K, $\varnothing = 0.1$ mm): the corresponding capillaries were filled in a glovebox at the PSI-SINQ facility with the same pre-treated powder used to fill the vanadium cans for the ND at the HRPT station. In this way, combined X-ray and neutron refinements on patterns collected on identically pre-treated powders were carried out.

3. Results and discussion

3.1. Crystal structure of LW(Mo)O

In Table 1, a summary of the Mo-substituted LWO samples [LW(Mo)O] investigated in this work is presented along with nominal and experimental (EPMA/XRD) compositions, possible secondary phases, techniques used and sample labels. The pre-characterization of the LW(Mo)O specimen series, including the supposed phase diagram, laboratory XRD patterns and thermogravimetric analyses, has been published elsewhere (Fantin *et al.*, 2017). It is recalled that all the specimens presented in this work (*cf.* Table 1) were produced by the citrate-complexation route based on the Pechini method (Pechini, 1967).

In the following, the structure of the LW(Mo)O specimens with particular attention to Mo20(1) and Mo20(2) is investigated through the combination of ND and HRXRD.

3.1.1. Method of the average neutron-scattering length. The two LW(Mo)O specimens with the highest Mo-substitution levels, Mo20(1) [$\text{La}_{5.64(4)}\text{W}_{0.809(7)}\text{Mo}_{0.191(2)}\text{O}_{12-\delta}$] and Mo20(2) [$\text{La}_{5.64(7)}\text{W}_{0.803(7)}\text{Mo}_{0.197(7)}\text{O}_{12-\delta}$] (see Table 1), were selected to be refined through the average scattering length

Table 2

Refined SOFs of the cation sites 4*a*, 4*b* and 48*h* of specimens Mo20(1) and Mo20(2) obtained through the average neutron-scattering length approach.

Results of all data sets collected at low temperatures for Mo20(2) (*T* = 10 and 30 K) and at *T* = 298 K for Mo20(1), as well as under the different atmospheres [dry(Ar) and D₂O(Ar/SA)], are listed. For comparison, the average SOFs of the LWO_P specimen and the calculated weighted average occupancies of Mo20(1) and Mo20(2) are also reported.

Temperature – atmosphere	SOF _{4<i>a</i>} ^W	SOF _{4<i>b</i>} ^{La₁}	SOF _{48<i>h</i>} ^{La₂}
Sample Mo20(2)			
10 K dry(Ar) ^{HRPT}	1.07 (2)	1.00 (1)	0.488 (2)
10 K D ₂ O(SA) ^{HRPT}	1.03 (2)	0.97 (1)	0.499 (2)
30 K dry(Ar) ^{D2B}	1.04 (3)	0.96 (1)	0.493 (3)
30 K D ₂ O(Ar) ^{D2B}	1.05 (3)	0.97 (2)	0.498 (3)
Average SOFs	1.05 (2)	0.98 (1)	0.494 (2)
Sample Mo20(1)			
298 K dry(Ar) ^{D2B}	1.07 (4)	1.00 (2)	0.494 (4)
298 K D ₂ O(Ar) ^{D2B}	1.07 (5)	1.00 (3)	0.496 (5)
Average SOFs	1.07 (3)	1.00 (2)	0.495 (3)
Sample LWO_P			
Average SOFs	0.99 (1)	0.99 (1)	0.486 (1)

approach, and the occupancy of the cation Wyckoff sites (4*a*, 4*b*, 48*h*) was compared with the results for the LWO_P specimen. As shown by Fantin *et al.* (2017), specimen Mo20(2) shows a tiny amount of the secondary phases La₂O₃ (<1 wt%) and La₆W₂O₁₅ (<1 wt%) but the composition of the main phase is the same within the error as that of specimen Mo20(1), which is single phase within the resolution of the XRD measurements. However, the amount of powder available for Mo20(2) is about 10 g compared with <2 g of the phase-purer Mo20(1) specimen, which makes Mo20(2) more suitable for temperature-dependent ND measurements in the temperature range 10 ≤ *T* ≤ 298 K. Specimen Mo20(1) was also measured with neutrons at *T* = 298 K at ILL because of the high flux available at D2B. No visible difference either in the neutron patterns of Mo20(1) and Mo20(2) or in the refinement results was ascertained. The results from average scattering length analyses of Mo20(1) and Mo20(2) specimens, the measuring temperatures, and the average site-occupancy factors (SOFs) are reported in Table 2.

ND revealed a 4*a* SOF of 1.05 (1) for Mo20(2) and 1.07 (3) for Mo20(1), resulting in an Mo amount on the 4*a* site of 12 (5) and 17 (7)% for Mo20(2) and Mo20(1), respectively. A plot of the average scattering length $\bar{b}_{4a}^{\text{exp}}$ for the LW(Mo)O series as a function of the amount of W substitution by Mo along with the composition results from EPMA is presented in Fig. 1. From the refined 4*a* SOFs listed in Table 2, the experimental average neutron-scattering length for Wyckoff site 4*a*, $\bar{b}_{4a}^{\text{exp}}$, can be calculated. Green squares represent average $\bar{b}_{4a}^{\text{exp}}$ values obtained from refinements performed on LWO_P-D₂O(SA) (*T* = 1.5 K) and Mo20(2)-dry(Ar)/D₂O(SA) specimens (*T* = 10 K) measured at HRPT, and from refinements performed on LWO_P-dry(Ar)/D₂O(Ar) specimens (*T* = 5 K) and Mo20(2)-dry(Ar)/D₂O(Ar) specimens (*T* = 30 K) measured at D2B. Cation SOFs were assumed to be inde-

pendent of the specific pre-treatment used. The $\bar{b}_{4a}^{\text{exp}}$ values obtained only by D2B data [Mo1, Mo5 and Mo20(1), *T* = 298 K] are represented by black triangles. The blue points in Fig. 1 were calculated under the assumption that the Mo amount measured by EPMA entirely occupies the 4*a* site. Red dashed lines represent statistical occupation of Mo atoms on the 4*a* site with maximum and minimum values corresponding to La/(W + Mo) = 5.8 and La/(W + Mo) = 5.4, respectively.

The two data points determined by EPMA corresponding to Mo10 and Mo15 specimens are reported in brackets because the refinements of ND patterns (*T* = 298 K) performed on Mo10 and Mo15 gave inconsistent results, which are not depicted in Fig. 1. The inconsistency is ascribed to the incomplete diffusion of the reactants during the sintering procedure [see Fantin *et al.* (2017) for details].

The linear fit in Fig. 1 was performed assuming that the 4*a* site was fully occupied for the non-substituted LWO_P. From the statistical occupation range of Mo atoms in the 4*a* site one can see the effect of the lower contrast between Mo and W, compared for instance with that between Re and W (Fantin *et al.*, 2016). The red dashed line corresponding to the maximum allowed statistical occupation of Mo atoms on the 4*a* site lies within the error on values assumed to correspond to full 4*a* occupation by Mo, which are therefore indistinguishable. From the linear fit on the experimental data (black short-dashed line in Fig. 1), it can be inferred that Mo does not fully occupy the 4*a* Wyckoff site, which is shared with W. However, as the fit lies on the minimum allowed statistical occupation, which corresponds to an La/(W + Mo) = 5.4 ratio, a firm

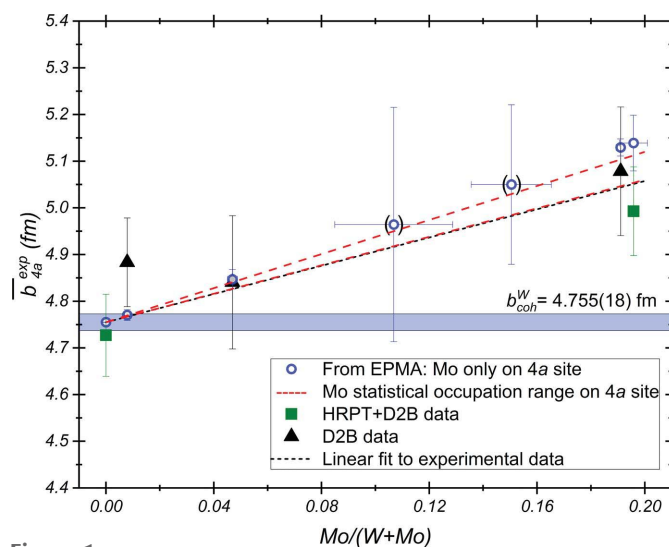


Figure 1

Average neutron-scattering length of the 4*a*-W₁ Wyckoff site, $\bar{b}_{4a}^{\text{exp}}$, for the LW(Mo)O series, as a function of W substitution by Mo [Mo/(W + Mo)]. Green squares and black triangles represent average $\bar{b}_{4a}^{\text{exp}}$ values obtained from refinements performed on specimens measured at HRPT and D2B, and on D2B only, respectively. Blue circles show the 4*a* site occupancy calculated under the assumption that the amount of Mo measured by EPMA entirely occupies the 4*a* site for each LW(Mo)O specimen. Red dashed lines represent the statistical occupation range of Mo atoms on the 4*a* site. The Mo10 and Mo15 data points are added in brackets (*cf.* text). The linear fit on the data uses direct *x*-weighing and the intercept is fixed to $\bar{b}_{4a}^{\text{exp}}(0) = 1$. The coherent-scattering length of W is depicted in a light blue colour.

Table 3

Refined SOFs of the cation sites *4a* and *48h* of the non-substituted LWO_P and the single-phase LW(Mo)O-D₂O(SA) specimens obtained through the average X-ray scattering power approach.

Patterns were collected with the cryojet at $T = 100$ K and without a sample environment at $T = 295$ K. Also given are the corresponding La/(W + Mo) ratio determined by EPMA, the amount of anti-site disorder, $W_2 + Mo_2$ on La_2 (at.% and e^- atom⁻¹), and the contributions of W_2 and Mo_2 on La_2 (e^- atom⁻¹) according to EPMA.

Samples in D ₂ O(SA) state, temperature	SOF _{4a} ^W	SOF _{48h} ^{La₂}	La/(W + Mo) EPMA	W ₂ + Mo ₂ on La ₂ (EPMA) (at.%)	W ₂ + Mo ₂ on La ₂ (EPMA) (e^- atom ⁻¹)	W ₂ , Mo ₂ on La ₂ (EPMA) (e^- atom ⁻¹)
LWO_P (295 K)	1.044 (2)	0.5076 (6)	5.56 (3)	3.66 (7)	2.46	2.46, 0
Mo1 (100 K)	1.027 (2)	0.5053 (7)	5.62 (3)	3.43 (7)	2.293	2.29, 0.003
Mo5 (100 K)	1.003 (2)	0.5037 (6)	5.64 (3)	3.42 (8)	2.28	2.23, 0.05
Mo20(1) (100 K)	0.927 (4)	0.5030 (13)	5.64 (3)	3.40 (9)	2.06	1.85, 0.21
Mo20(2) (295 K)	0.923 (2)	0.5028 (6)	5.64 (5)	3.42 (17)	2.06	1.85, 0.21

statement about statistical substitution of W by Mo on *4a* cannot be made on the basis of these data only.

Despite being single-phase specimens, Mo1 and Mo5 reveal large errors in the occupancies because of the low amount of material available: <1 g per dry(Ar)/D₂O(Ar) state. Such problems do not apply in HRXRD measurements because of the high photon flux available at synchrotrons, as sample amounts of the order of mg are sufficient. Moreover, Mo ($Z_{Mo} = 42$) has an electron density substantially different from that of W ($Z_W = 74$), resulting in a higher relative contrast $[Re(f)^W - Re(f)^{Mo}]/Re(f)^W \simeq 47\%$ calculated for the +6 ions than that for ND, $(b_{coh}^W - b_{coh}^{Mo})/b_{coh}^W \simeq 29\%$. Therefore, the LW(Mo)O series is particularly suitable for average X-ray scattering power studies, presented in the following.

3.1.2. Method of the average X-ray scattering power. The method of the average X-ray scattering power was used complementarily to the method of the average neutron-scattering length in order to prove independently that Mo substitutes W in both *4a* and *48h* Wyckoff sites. Measurements were collected below the Mo *K* edge at $E = 19.9$ keV, in order to enhance the contrast between Mo and W from 47%, far from any Mo or W absorption edges, to about 54% at $E = 19.9$ keV. The measurements were performed in a cryostat down to $T = 10$ K to reduce thermal atomic vibrations. In addition, measurements were performed outside the cryostat at $T = 100$ K using a cryojet and at $T = 295$ K to enhance the alignment precision (*i.e.* reduce capillary wobbling) and to reduce noise from the sample environment, thus improving the refinement accuracy. The resulting X-ray average scattering powers of the cation sites *4a* and *48h* refined for the phase-pure LW(Mo)O specimens LWO_P, Mo1, Mo5 and Mo20(1) are summarized in Table 3. The SOF of the *4b* site was fixed to $SOF_{4b}^{La_1} = 1$ (see discussion below). Moreover, the corresponding La/(W + Mo) ratio from EPMA [see Table 1 and Fantin *et al.* (2017)], the theoretical amount of anti-site disorder calculated according to $La_{28-x}(WMo)_{4+x}O_{54+\delta}$ and the theoretical electron number corresponding to the amount of anti-site disorder on the *48h* position are also presented ($W_2 + Mo_2$ on La_2 , in at.% and e^- atom⁻¹) and split into atomic contributions (W_2, Mo_2 on La_2 , in e^- atom⁻¹).

The occupancy factor of W on the *4a* site listed in Table 3 decreases with increasing Mo concentration because of the lower number of electrons per atom for Mo $[Re(f)_{19.9\text{keV}}^{Mo6+} \simeq$

$31.4 e^-$ atom⁻¹] compared with W $[Re(f)_{19.9\text{keV}}^{W6+} \simeq 67.3 e^-$ atom⁻¹], confirming the result obtained from the average neutron-scattering length procedure (see Table 2 and Fig. 1). This result provides an independent proof that Mo substitutes W on the *4a* Wyckoff site. Moreover, in the LWO_P, Mo1 and Mo5 specimens, the *4a* site seems to be slightly overestimated. This has been found for both LWO_P-dry(Ar) and LWO_P-D₂O(SA) specimens (Fantin, 2016; Scherb *et al.*, 2016). The *4b* site has been assumed to be fully occupied by an La₁ atom independent of Mo concentration because of the very different ionic radii and the different possible coordination numbers between La $[R_i(La)_{3+}^{8fold} = 1.16 \text{ \AA}]$ and Mo $[R_i(Mo)_{3+}^{6fold} = 0.69 \text{ \AA}]$. A decreasing trend is also seen for the refined *48h* occupancy as a function of Mo concentration. However, in order to understand and discuss correctly the *48h* average X-ray scattering power, four columns were added to Table 3 and copied into the supporting information along with a detailed explanation. The occupancy of the *48h* position is difficult to predict, as it depends on the La/(W + Mo) ratio and is also correlated to the other occupancies. However, combined experimental and theoretical results indicate that Mo atoms substitute W on both its *48h* and *4a* sites, which is explained as follows. Theoretical calculations to estimate $Re(f)$ were performed considering the *48h* anti-site concentration as fully occupied by W and also supposing the Mo atoms entirely occupy the *4a* Wyckoff site, similar to what has been shown in Fig. 1 for neutrons. Refinement results (full symbols) and theoretical calculations (open symbols) converted into $Re(f)$ are presented in Fig. 2. The experimental value of $Re(f)$ was obtained from the refined SOFs shown in Table 3. The theoretical calculations of $Re(f)$ were performed according to the atomic form-factor tabulation given by Chantler (1995). As explained by Chantler (1995) and in the NIST documentation (NIST, 2003), the uncertainty was taken as 1% of the calculated value. Considering that the X-ray energy used ($E = 19.9$ keV) is far away from any La edge and that about 96.5 at.% of the *48h* site is occupied by La atoms, an uncertainty of 0.1% on the calculated $Re(f)$ for the *48h* site is also reported in Fig. 2.

In Fig. 2, the decreasing trend of $Re(f)$ for the *4a* Wyckoff site with increasing Mo concentration is clearly visible (black dashed line), comparable with ND results of Fig. 1. However, the refined value of $Re(f)$ for the *4a* site is higher than the

attempted. The metal and the oxygen O_1 SOFs were fixed to the values obtained with HRXRD and ND refinements, respectively. The observed X-ray and ND intensities, calculated intensities, and their difference are plotted for Mo20(2)-dry(Ar) patterns in Figs. 3 and 4, respectively, as a function of q in the refined region. No appreciable difference was observed in the Mo20(2)-D₂O(SA) patterns, which are not shown for the sake of brevity. The results of the fits are shown in Table 4 along with the obtained lattice parameters and residuals.

In Fig. 5, selected metal–oxygen bond lengths obtained from neutron refinements and combined X-ray/neutron refinements are presented as a function of temperature, *i.e.* the $4a-96k$ (W_1/Mo_1-O_1), $4b-32f$ (La_1-O_2) and $48h-32f$ distances ($La_2/W_2/Mo_2-O_2$). The corresponding neutron diffractograms are reported in the supporting information for completeness (Fig. S1). The bond lengths between the $48h$ and $96k$ Wyckoff sites are not treated because of the high disorder of both the $48h$ and $96k$ Wyckoff sites. The $48h-96k$ bonds in LW(Mo)O are even more difficult to discuss compared with

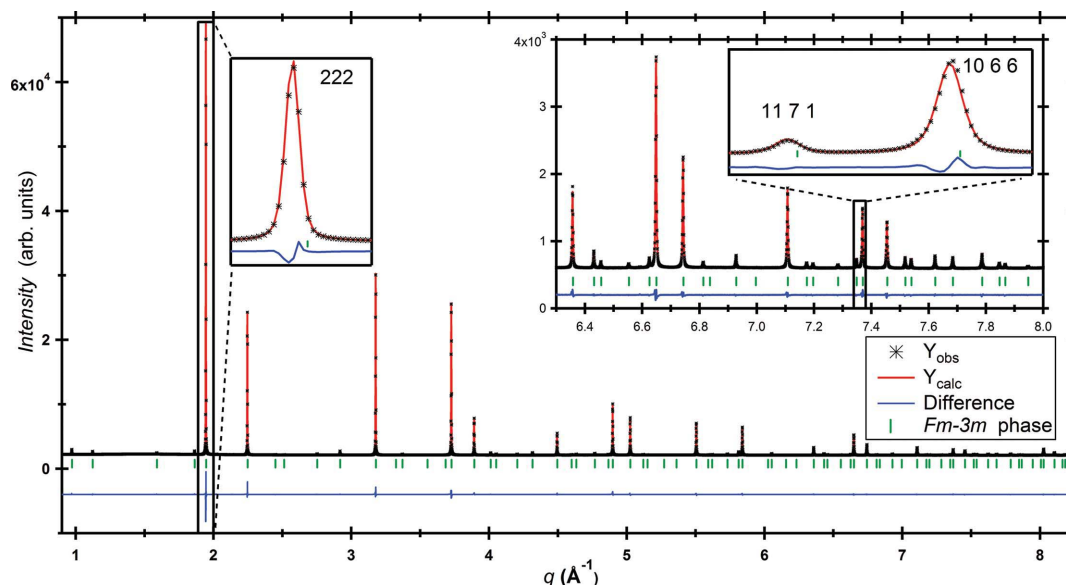


Figure 3 HRXRD intensity plots of Mo20(2)-dry(Ar), $La_{5.64}W_{0.803}Mo_{0.197}O_{12-\delta}$, data collected at $T = 295$ K at the MS beamline (SLS), as a function of the momentum transfer (black “*” markers), calculated data (red line), and difference of the measured and calculated data (blue line). In the insets, the high-angle data ($6.3 \leq q \leq 8 \text{ \AA}^{-1}$) are magnified, as well as three chosen diffraction peaks, one at low scattering angles ($q \approx 1.95 \text{ \AA}^{-1}$, $hkl = 222$) and the last two at high scattering angles ($q \approx 7.34 \text{ \AA}^{-1}$, $hkl = 1171$ and $q \approx 7.37 \text{ \AA}^{-1}$, $hkl = 1066$). Observed, calculated and difference lines are shifted for better peak visualization.

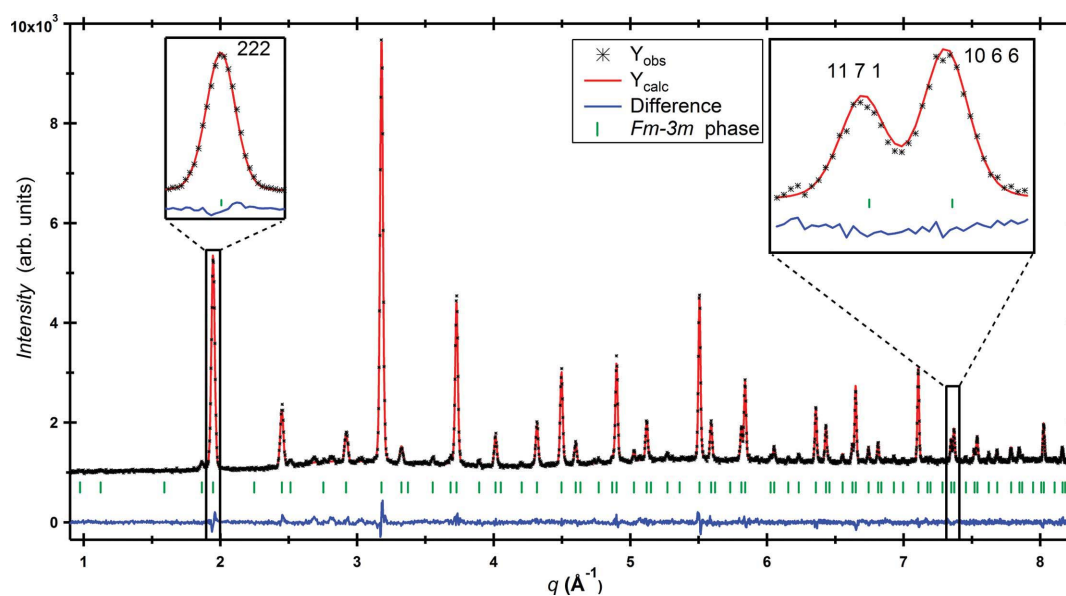


Figure 4 ND intensity plots of Mo20(2)-dry(Ar), $La_{5.64}W_{0.803}Mo_{0.197}O_{12-\delta}$, data collected at $T = 295$ K at the HRPT instrument (SINQ), as a function of the momentum transfer (black “*” markers), calculated data (red line), and difference of the measured and calculated data (blue line). In the insets, three chosen diffraction peaks are presented, one at low scattering angles ($q \approx 1.95 \text{ \AA}^{-1}$, $hkl = 222$) and the last two at high scattering angles ($q \approx 7.34 \text{ \AA}^{-1}$, $hkl = 1171$ and $q \approx 7.37 \text{ \AA}^{-1}$, $hkl = 1066$). Observed, calculated and difference lines are shifted for better peak visualization.

Table 4

Fractional atomic coordinates (x, y, z), SOFs and the equivalent displacement parameters (U_{eq}), for Mo20(2) ($\text{La}_{5.64}\text{W}_{0.803}\text{Mo}_{0.197}\text{O}_{12-\delta}$) dry(Ar) and $\text{D}_2\text{O}(\text{SA})$ from combined ND (HRPT at SINO, $T = 295$ K) and HRXRD (MS at SLS, $T = 295$ K) refinements.

All the displacement parameters U_{eq} are multiplied by a factor of 100. The refinements were performed with space group $Fm\bar{3}m$. The lattice parameters and the residuals are also reported. The anisotropic displacement parameters U_{xy} ($x, y = 1, 2, 3$) are reported in the CIF.

Atom	Site	x	y	z	$U_{eq}(\text{\AA}^2)$	SOF
La ₁	Dry	4b	0.5	0.5	1.14 (3)	1†
	D ₂ O					
W ₁	Dry	4a	0	0	0.57 (2)	0.832 (1)‡
	D ₂ O					
Mo ₁	Dry	4a	0	0	0.57 (2)	0.168 (1)‡
	D ₂ O					
La ₂	Dry	48h	0	0.23584 (4)	0.23584 (4)	0.4815 (6)‡
	D ₂ O			0.23538 (3)	0.23538 (3)	
W ₂	Dry	48h	0	0.23584 (4)	0.23584 (4)	0.0120 (2)‡
	D ₂ O			0.23538 (3)	0.23538 (3)	
Mo ₂	Dry	48h	0	0.23584 (4)	0.23584 (4)	0.0064 (2)‡
	D ₂ O			0.23538 (3)	0.23538 (3)	
O ₁	Dry	96k	0.1112 (1)	0.1112 (1)	0.0664 (2)	0.25§
	D ₂ O		0.1115 (1)	0.1115 (1)	0.0656 (2)	0.25§
O ₂	Dry	32f	0.3661 (1)	0.3661 (1)	0.3661 (1)	0.968 (3)
	D ₂ O		0.3661 (1)	0.3661 (1)	0.3661 (1)	1.92 (2)

	Lattice parameter (Å)	T (K)	R_{exp} (%)	R_{wp} (%)	χ^2	R_B (%)
Dry	11.18018 (1)	295	5.64	4.42	1.63	1.76
D ₂ O	11.18529 (1)		6.43	5.08	1.61	2.16

† Not refined. ‡ Taken from HRXRD simultaneous refinements. § Fixed from ND simultaneous refinements (*cf.* text).

the non-substituted LWO system because of the additional Mo atoms in both the 48h and 4a Wyckoff sites. For details the reader is referred to the local structure of LWO reported by Scherb *et al.* (2016).

Interpolations of data points were only performed on results from D2B because of the larger number of patterns compared with HRPT. However, the latter values are reported in Fig. 5 for completeness and marked by (*). As refinements

on HRPT data were not possible with all anisotropic displacement parameters (ADPs) free, the absolute values of the extracted bond lengths cannot be compared with D2B data without considering error propagation. A factor of 2 to the bond-length standard deviation (*i.e.* 2σ) was assumed to be a good approximation. Bond-length values obtained from the four-pattern combined X-ray and neutron refinements (stars in Fig. 5) fit very well with the trend of D2B values, remaining compatible to the linear regression lines. The bond lengths of La₁–O₂ and 48h–O₂ given in Fig. 5 increase with temperature, as shown by positive slopes in the linear fitting. On the other hand, 4a–O₁ bond lengths apparently decrease with increasing temperature. As shown elsewhere for the LWO system (Fantin *et al.*, 2016; Fantin, 2016) angular oscillations of O₁ around W₁ create an apparent bond shortening with increasing temperature, which is also visible for the 4a–O₁ bond lengths of the Mo20(2) specimen in Fig. 5. No

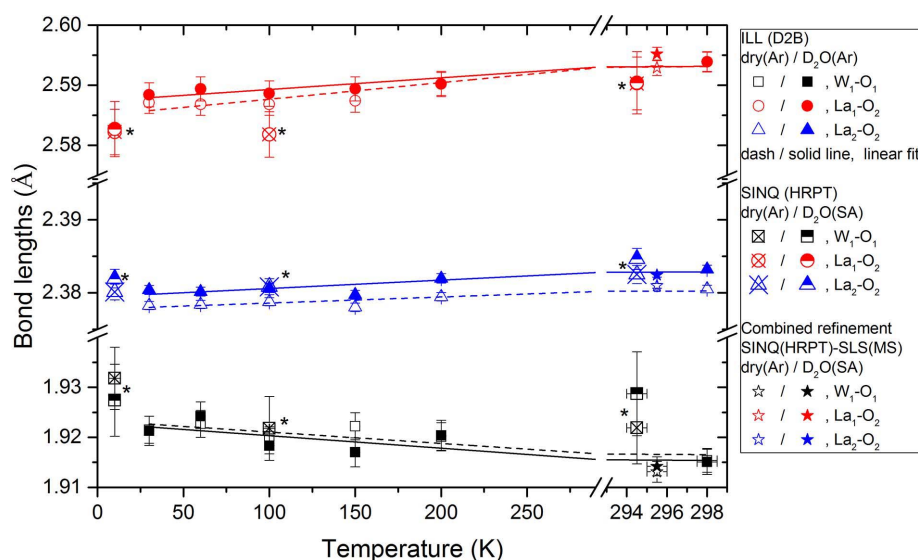


Figure 5 Selected bond lengths from refinements of ND data of the Mo20(2) specimen at HRPT, dry(Ar)/D₂O(SA), and D2B, dry(Ar)/D₂O(Ar), experimental stations as a function of temperature. Linear fits to the data were performed including only D2B data. Dashed and solid lines represent fits to the Mo20(2)-dry(Ar) and Mo20(2)-D₂O(Ar) data, respectively. HRPT data (*) could not be refined with all ADPs free. The standard deviation of the corresponding bond lengths extracted was doubled (*cf.* text). Star symbols represent bond lengths extracted from the combined HRPT/SLS refinements described above (see Figs. 3 and 4 and Table 4). Data points obtained from combined refinements and from HRPT only at $T = 295$ K were shifted by 0.5 and -0.5 K, respectively, for a better visualization.

Table 5

The intercept values ($T = 0$ K) of linear fits performed for different metal–oxygen bond lengths of Mo20(2)-dry(Ar)/D₂O(Ar) specimens as a function of temperature (see Fig. 5).

Mo20(2)	Bond length (Å) dry(Ar)	Bond length (Å) D ₂ O(Ar)
4a–O ₁	1.923 (1)	1.923 (2)
La ₁ –O ₂	2.585 (1)	2.587 (1)
48h–O ₂	2.3778 (4)	2.3794 (6)

change upon deuteration is noticed in the 4a–O₁ bond lengths for any temperature, so deuteration does not change the first shell of the 4a Wyckoff site (W₁/Mo₁), octahedrally coordinated with oxygen atoms (O₁). Octahedral coordination of the 4a Wyckoff site (W₁/Mo₁) is confirmed for both Mo20(2)-dry(Ar) and -D₂O(SA) by the SOF values of the O₁ sites simultaneously refined for different temperature patterns. Contrary to the 4a–O₁ bonds, the La₁–O₂ and 48h–O₂ bond lengths slightly differ upon deuteration (see linear fits in Fig. 5). The intercepts with the y axis (*i.e.* $T = 0$ K) of the linear fits carried out on bond lengths as a function of temperature in Fig. 5 are presented in Table 5.

It is recalled that in the $Fm\bar{3}m$ model used O₂ (32f site: x, x, x) can move along the [111] direction towards or away from the La₁-4b site. As the La₁–O₂ bond length depends on the ionic radii and the coordination of La, an eightfold coordinated La ion has a larger bond length with O₂ compared with a sevenfold coordinated La ion. Such a tiny difference of 0.002 (2) Å is rationalized by the low number of vacant sites that it is possible to fill, on average about 0.5 per unit cell. In general, because of geometrical restrictions, higher coordination yields larger bond lengths, as predicted and rationalized by Pauling for crystal structures of ionic compounds (Pauling, 1929). The second of his rules states that if z is the electronic charge of a cation and N its coordination number, the bond strength S is defined as $S = z/N$. As the charge of lanthanum in ionic compounds is $z_{La} = +3$ (Shannon, 1976), it follows that S increases with decreasing N . It also follows that the bond length, inversely proportional to the bond strength, increases with the coordination number N . Even if the O₂ atoms are constrained to move in the (x, x, x) direction and thus are not free to rearrange, a vacancy at the 32f site should induce a decrease in the bond length 4b–32f of dry(Ar) specimens, appreciable in Fig. 5 below $T = 150$ K (full red circles). The decrease of the 4b–32f bond-length difference between dry(Ar) and D₂O(Ar) conditions seen at $T > 150$ K may be either masked by increasing disorder and thermal vibration effects or rationalized by the repulsion between the 32f and the 48h site. Understanding 48h (La₂/W₂/Mo₂)–O₂ bonding is more difficult because of the number of atoms involved and the free refineable positions of 48h (0, y, y) and 32f (x, x, x) which give a relative displacement of one atom with respect to the other. However, the same reasoning as for the La₁–O₂ bond can be applied for (La₂/W₂/Mo₂)–O₂ bonds. Firstly, the 48h site is assumed to be occupied only by La₂ atoms (see Table 3). Then, La₂ is sevenfold coordinated if there are no vacancies in the 32f position and sixfold coordinated if one

vacancy occupies the 32f site. According to Pauling's bond-strength definition, a decrease in coordination from sevenfold to sixfold of La ($z_{La} = +3$) would induce a bond-length shortening with the surrounding oxygen atoms.

As a final point, the temperature dependence of some of the LW(Mo)O-dry(SA) specimens [Mo5, Mo20(1), LWO_P] measured at SLS-MS in the temperature range $T = 10$ –295 K by HRXRD is presented in Fig. 6. Data were collected at $T = 10, 30, 60, 100, 150, 200, 240, 270$ and 295 K. Specimen dilution with NIST Si640d powder was carried out in order to reduce specimen absorption while using larger capillaries ($\varnothing = 0.2$ mm), necessary for better alignments in the cryostat, and for calibration purposes. As small capillary displacement during cooling in the cryostat took place, the lattice parameters of Si640d powder were used as an internal reference to refine the capillary position at different temperatures. Si640d lattice parameters were calculated through linear thermal expansion of Si, reported by Batchelder & Simmons (1964), and by further comparison with measured lattice-parameter values of pure Si at different temperatures given by Shah (1971). In short, Si lattice parameters at the measured temperatures were calculated, capillary x and y displacements (z is the beam direction) were accordingly refined, and the calibrated lattice parameters for Mo20(1), Mo5 and LWO_P specimens were finally obtained, keeping the capillary position fixed to the values obtained for Si640d.

All the LeBail fits performed for LWO_P, Mo5 and Mo20(1) specimens yield $0.5 \leq R_{\text{exp}} \leq 0.7\%$ and $1.3 \leq R_{\text{wp}} \leq 1.9\%$ resulting in an average χ^2 of between 2 and 4, thus proving the reliability of the fits. The lattice parameters of Mo5 and Mo20(1)-dry(SA) decrease with decreasing temperature and level off in the low-temperature region, similar to LWO as

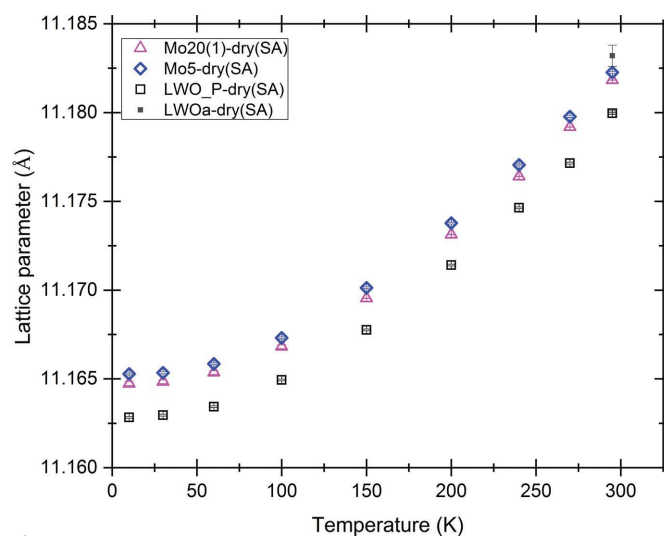


Figure 6 Lattice parameters of LWO_P (La_{5.56}W_{0.12}– δ , black squares), Mo5 (La_{5.64}W_{0.95}Mo_{0.05}O_{12– δ} , blue diamonds) and Mo20(1) (La_{5.64}W_{0.81}Mo_{0.19}O_{12– δ} , purple triangles) specimens in dry(SA) as a function of temperature between $T = 10$ K and $T = 295$ K. In order to consider the contribution of the La/W ratio in lattice-parameter expansion, the calculated lattice parameter of a fictitious LWO specimen labelled LWOa (La/W_{LWOa} = 5.64, *cf.* text) was added. The associated uncertainties for HRXRD data are smaller than the data points.

shown in Fig. 6 and in the literature (Fantin *et al.*, 2016; Fantin, 2016). Because of the different La/W ratios between LWO_P ($\text{La}/\text{W}_{\text{LWO_P}} = 5.56$), Mo5 [$\text{La}/(\text{W} + \text{Mo})_{\text{Mo5}} = 5.64$ (3)] and Mo20(1) [$\text{La}/(\text{W} + \text{Mo})_{\text{Mo20(1)}} = 5.64$ (4)] (see Fantin *et al.*, 2017 and Table 1), the absolute lattice-parameter values cannot be compared directly. As the La atoms are the largest in the crystal structure [$R_1(\text{La})_{3+}^{\text{fold}} = 1.16$ Å] they contribute the most to the unit-cell size. Specimens with higher La/W ratios show a larger number of vacancies in the crystal structure, as well. For this reason, the lattice parameter of a non-substituted LWO specimen, LWO55, with slightly higher ratio than the Mo-substituted specimens, $\text{La}/\text{W}_{\text{LWO55}} = 5.69$ (4), was obtained by conventional XRD, $a_{\text{LWO55-dry(SA)}} = 11.1869$ (1) Å, and related to the LWO_P-dry(SA) lattice parameter, $a_{\text{LWO_P-dry(SA)}} = 11.1817$ (1) Å, assessed under the same experimental conditions. From a linear interpolation between these two lattice parameters, the lattice parameter of a fictitious LWO (LWOa) specimen with the same La/W ratio as the Mo-substituted specimens, $\text{La}/\text{W}_{\text{LWOa}} = 5.64$, was obtained and added in Fig. 6. A small offset, found to be about 0.001 Å, was considered when comparing conventional XRD with HRXRD data, assuming that the HRXRD data are more reliable. At this point, a comparison between the different specimens reported in Fig. 6 can be carried out. In dry(SA) conditions, by increasing the substitution of W by Mo, the lattice shrinks. The difference in lattice parameter at $T = 295$ K between the LWOa specimen and Mo5 is $\Delta(a_{\text{LWOa}} - a_{\text{Mo5}}) = 10$ (5) $\times 10^{-4}$ Å, while between Mo5 and Mo20(1) the difference is $\Delta[a_{\text{Mo5}} - a_{\text{Mo20(1)}}] = 4$ (1) $\times 10^{-4}$ Å. The tiny decrease of lattice parameters found upon increasing the Mo content is rationalized by the ionic radius of Mo [$R_1(\text{Mo})_{6+}^{\text{fold}} = 0.59$ Å], which is only slightly smaller than that of W [$R_1(\text{W})_{6+}^{\text{fold}} = 0.60$ Å] if sixfold coordination and a +6 oxidation state for both elements are assumed. This assumption follows the oxidizing conditions, dry(SA), used in the pre-treatment. Clearly, the lattice expansion is a function as well of the used pre-treatment conditions, or, in other words, of the number of oxygen vacancies. In recent work (Fantin *et al.*, 2017), lattice parameters of Mo20(1) in dry(Ar) state [$a_{\text{Mo20(1)-dry(Ar)}} = 11.1791$ (1) Å] and in D₂O(Ar) state [$a_{\text{Mo20(1)-D2O(Ar)}} = 11.1838$ (1) Å] were reported. The Mo20(1)-dry(SA) lattice-parameter value remains in between [$a_{\text{Mo20(1)-dry(SA)}} = 11.18120$ (1) Å]. Even if one takes into account the changes caused by Mo substitution at the same oxidation state [$\Delta(a_{\text{Mo5}} - a_{\text{Mo20(1)}}) = 4$ (1) $\times 10^{-4}$ Å], one finds that oxygen sites (vacant or filled) play a major role in lattice expansion. In Fig. 5 and Table 5, and in other publications as well (Fantin *et al.*, 2016; Fantin, 2016), it is reported that substituted and non-substituted LnWO (Ln = La, Nd) oxygen vacancy sites occupy the 32*f* (O₂) Wyckoff sites. By comparing the bond lengths of La₁–O₂ obtained at room temperature by HRXRD for the specimens with the same composition, Mo20(2) and Mo20(1), it is found that La₁–O₂ bond lengths increase with increasing pO₂ and pD₂O, in line with expectations. The lowest and the highest La₁–O₂ bond-length values correspond to dry(Ar) and D₂O(SA) conditions, La₁–O₂ Mo20(2)-dry(Ar) = 2.600 (2) Å and La₁–O₂ Mo20(2)-D₂O(SA) = 2.621 (2) Å, respectively. The

intermediate La₁–O₂ bond-length value corresponds to pre-treatments carried out in dry(SA) conditions, La₁–O₂ Mo20(1)-dry(SA) = 2.606 (3) Å. For obtaining the above-mentioned bond lengths, only SLS-MS high-resolution X-ray data were used for comparison purposes.

4. Summary and conclusions

In this work, the structure of Mo-substituted lanthanum tungstates ($\text{La}_{5.4}\text{W}_{1-y}\text{Mo}_y\text{O}_{12-\delta}$, $0 \leq y \leq 0.2$) was investigated using HRXRD and ND at temperatures between 10 and 298 K. Specimens were also studied as a function of pre-treatments, *i.e.* they were dried and humidified under argon stream [dry(Ar), D₂O(Ar)] and synthetic air stream [dry(SA), D₂O(SA)]. Using the average neutron-scattering length and average X-ray scattering power methods, it has been demonstrated that Mo substitutes W on both 4*a* and 48*h* Wyckoff sites, confirming previous results on Mo-substituted LWO (Magrasó & Frontera, 2016), and in a statistical fashion, such as for Re-substituted LWO (Fantin *et al.*, 2016). Simultaneous Rietveld refinements of high-resolution X-ray data were used to determine the metal SOFs, while simultaneous Rietveld refinements of ND data were used to establish the oxygen SOFs. Simultaneous Rietveld refinements combining high-resolution X-ray diffraction and neutron-diffraction patterns allowed the complete structural information of $\text{La}_{5.6}\text{W}_{0.8}\text{Mo}_{0.2}\text{O}_{12-\delta}$ to be accessed. From bond-length investigation as a function of temperature and pre-treatment [dry(Ar), wet(D₂O)], oxygen vacancies have been located on the 32*f* Wyckoff site, bonded to the 48*h* Wyckoff site. Libration movements of oxygen atoms on 96*k* Wyckoff sites around W located on 4*a* Wyckoff sites have been found as well, in agreement with previous results on non-substituted and Re-substituted LWO materials (Fantin *et al.*, 2016). Finally, lattice parameters on substituted LWO systems can be compared only when the La/W ratio lies within the error. The bond length between the 4*b* site occupied by La and the oxygen deficient 32*f* site, where the oxygen vacancies are located, is found to enlarge with increasing pO₂ and pD₂O, as oxygen vacancies in the crystal structure are filled by O and OD groups, respectively.

Acknowledgements

We thank the Institut Laue–Langevin (Fantin *et al.*, 2014), the Paul Scherrer Institute for the allocation of beamtime, and the beamline scientists E. Suard (D2B–ILL), V. Pomjakushin (HRPT–SINQ) and N. Casati (MS–SLS). We also thank J. Nissen (Technical University of Berlin) for conducting the EPMA measurements, and C. Leistner and C. Förster (Helmholtz-Zentrum Berlin) for help in performing TG and XRD experiments and in sample preparation.

Funding information

The Helmholtz Association funded this work through the Helmholtz Alliance MEM-BRAIN (Initiative and Networking Fund).

References

- Batchelder, D. N. & Simmons, R. O. (1964). *J. Chem. Phys.* **41**, 2324–2329.
- Bruker (2008). *DIFFRACplus Evaluation Package EVA14*. Release 15 July 2008. Bruker AXS GmbH, Karlsruhe, Germany.
- Chantler, C. (1995). *J. Phys. Chem. Ref. Data*, **24**, 71–643.
- Chen, Y., Cheng, S. F., Chen, L., Wei, Y. Y., Ashman, P. J. & Wang, H. H. (2016). *J. Membr. Sci.* **510**, 155–163.
- Coelho, A. A. (2018). *J. Appl. Cryst.* **51**, 210–218.
- Dahl, P. I., Lein, H. L., Yu, Y. D., Tolchard, J., Grande, T., Einarsrud, M. A., Kjølsest, C., Norby, T. & Haugsrud, R. (2011). *Solid State Ionics*, **182**, 32–40.
- Erdal, S., Kalland, L. E., Hancke, R., Polfus, J., Haugsrud, R., Norby, T. & Magrasó, A. (2012). *Int. J. Hydrogen Energy*, **37**, 8051–8055.
- Escolástico, S., Seeger, J., Roitsch, S., Ivanova, M., Meulenberg, W. A. & Serra, J. M. (2013). *ChemSusChem*, **6**, 1523–1532.
- Escolástico, S., Somacescu, S. & Serra, J. M. (2014). *Chem. Mater.* **26**, 982–992.
- Escolástico, S., Somacescu, S. & Serra, J. M. (2015). *J. Mater. Chem. A*, **3**, 719–731.
- Evans, J. S. O. (2010). *Mater. Sci. Forum*, **651**, 1–9.
- Fantin, A. (2016). PhD thesis, Technische Universität Berlin, Germany.
- Fantin, A., Escolástico, S., Scherb, T., Schumacher, G. & Suard, E. (2014). *Characterization of Substituted Proton Conductor Materials $LaW_{(1-x)}M_{(x)}O_{12-\delta}$ ($M = Mo, Re; x=0, 0.01, 0.05, 0.1, 0.15, 0.2$)*, Institut Laue–Langevin (ILL), <http://doi.ill.fr/10.5291/ILL-DATA.5-23-661>.
- Fantin, A., Scherb, T., Seeger, J., Schumacher, G., Gerhards, U., Ivanova, M. E., Meulenberg, W. A., Dittmeyer, R. & Banhart, J. (2016). *J. Appl. Cryst.* **49**, 1544–1560.
- Fantin, A., Scherb, T., Seeger, J., Schumacher, G., Gerhards, U., Ivanova, M. E., Meulenberg, W. A., Dittmeyer, R. & Banhart, J. (2017). *Solid State Ionics*, **306**, 104–111.
- Fischer, P., Frey, G., Koch, M., Könnecke, M., Pomjakushin, V., Schefer, J., Thut, R., Schlumpf, N., Bürge, R., Greuter, U., Bondt, S. & Berruyer, E. (2000). *Physica B*, **276–278**, 146–147.
- Fontaine, M. L., Larring, Y., Norby, T., Grande, T. & Bredesen, R. (2007). *Ann. Chim. Sci. Mater.* **32**, 197–212.
- Furrer, A., Mesot, J. & Strässle, T. (2009). *Neutron Scattering in Condensed Matter Physics*. London: World Scientific.
- Genovese, A., Contrisciani, N., Ortenzi, F. & Cazzola, V. (2011). *Int. J. Hydrogen Energy*, **36**, 1775–1783.
- Haile, S. M., Staneff, G. & Ryu, K. H. (2001). *J. Mater. Sci.* **36**, 1149–1160.
- Haugsrud, R. (2007). *Solid State Ionics*, **178**, 555–560.
- Hewat, A. W. & Heathman, S. (1984). *Acta Cryst.* **A40**, C364.
- Ivanova, M. E., Escolástico, S., Balaguer, M., Palisaitis, J., Sohn, Y. J., Meulenberg, W. A., Guillon, O., Mayer, J. & Serra, J. M. (2016). *Sci. Rep.* **0**, 34773.
- Iwahara, H. (1988). *J. Electrochem. Soc.* **135**, 529–533.
- Iwahara, H., Esaka, T., Uchida, H. & Maeda, N. (1981). *Solid State Ionics*, **3–4**, 359–363.
- Kim, M., Sohn, Y.-J., Cho, C.-W., Lee, W.-Y. & Kim, C.-S. (2008). *J. Power Sources*, **176**, 529–533.
- Kjølsest, C., Wang, L. Y., Haugsrud, R. & Norby, T. (2010). *Solid State Ionics*, **181**, 1740–1745.
- Larson, A. C. & Von Dreele, R. B. (2004). Report LAUR 86–748. Los Alamos National Laboratory, New Mexico, USA.
- Lin, S. Y. (2002). *Fuel*, **81**, 2079–2085.
- Magrasó, A. (2013). *J. Power Sources*, **240**, 583–588.
- Magrasó, A. & Frontera, C. (2016). *Dalton Trans.* **45**, 3791–3797.
- Magrasó, A., Kjølsest, C., Haugsrud, R. & Norby, T. (2012). *Int. J. Hydrogen Energy*, **37**, 7962–7969.
- Niknam, T., Bornapour, M., Ostadi, A. & Gheisari, A. (2013). *J. Power Sources*, **239**, 513–526.
- NIST (2003). *X-ray Form Factor, Attenuation, and Scattering Tables*, <http://physics.nist.gov/PhysRefData/FFast/Text2000/sec02.html>.
- Norby, T. (1999). *Solid State Ionics*, **125**, 1–11.
- Norby, T. (2000). *Solid State Ionics*, **136–137**, 139–148.
- Norby, T. & Haugsrud, R. (2008). *Membranes for Energy Conversion*, pp. 169–216. Weinheim: Wiley-VCH Verlag.
- Pauling, L. (1929). *J. Am. Chem. Soc.* **51**, 1010–1026.
- Pechini, M. P. (1967). US Patent 3330697A.
- Quarez, E., Oumellal, Y. & Joubert, O. (2013). *Fuel Cells*, **13**, 34–41.
- Rebollo, E., Mortalò, C., Escolástico, S., Boldrini, S., Barison, S., Serra, J. M. & Fabrizio, M. (2015). *Energ. Environ. Sci.* **8**, 3675–3686.
- Ricote, S., Bonanos, N., Wang, H. J. & Haugsrud, R. (2011). *Solid State Ionics*, **185**, 11–17.
- Scherb, T., Kimber, S. A. J., Stephan, C., Henry, P. F., Schumacher, G., Escolástico, S., Serra, J. M., Seeger, J., Just, J., Hill, A. H. & Banhart, J. (2016). *J. Appl. Cryst.* **49**, 997–1008.
- Seeger, J., Ivanova, M. E., Meulenberg, W. A., Sebold, D., Stöver, D., Scherb, T., Schumacher, G., Escolástico, S., Solís, C. & Serra, J. M. (2013). *Inorg. Chem.* **52**, 10375–10386.
- Shah, J. S. (1971). PhD thesis, University of Missouri, USA.
- Shannon, R. D. (1976). *Acta Cryst.* **A32**, 751–767.
- Simpson, A. P. & Lutz, A. E. (2007). *Int. J. Hydrogen Energy*, **32**, 4811–4820.
- Sorensen, B. (2007). *Int. J. Hydrogen Energy*, **32**, 1597–1604.
- Stephan, C., Scherb, T., Kaufmann, C. A., Schorr, S. & Schock, H. W. (2012). *Appl. Phys. Lett.* **101**, 101907.
- Willmott, P. R., Meister, D., Leake, S. J., Lange, M., Bergamaschi, A., Böge, M., Calvi, M., Cancellieri, C., Casati, N., Cervellino, A., Chen, Q., David, C., Flechsig, U., Gozzo, F., Henrich, B., Jäggi-Spielmann, S., Jakob, B., Kalichava, I., Karvinen, P., Krempasky, J., Lüdeke, A., Lüscher, R., Maag, S., Quitmann, C., Reinle-Schmitt, M. L., Schmidt, T., Schmitt, B., Streun, A., Vartiainen, I., Vitins, M., Wang, X. & Wulschleger, R. (2013). *J. Synchrotron Rad.* **20**, 667–682.
- Toby, B. H. (2001). *J. Appl. Cryst.* **34**, 210–213.
- Zayas-Rey, M. J., dos Santos-Gómez, L., Marrero-López, D., León-Reina, L., Canales-Vázquez, J., Aranda, M. A. G. & Losilla, E. R. (2013). *Chem. Mater.* **25**, 448–456.
- Zeng, K. & Zhang, D. K. (2010). *Prog. Energy Combust. Sci.* **36**, 307–326.